Article

Effects of Heat Treatment of Selective Laser Melting Printed Ti-6Al-4V Specimens on Surface Texture Parameters and Cell Attachment

Pei-Wen Peng [1], Jen-Chang Yang [2], Wei-Fang Lee [1], Chih-Yuan Fang [3,4], Chun-Ming Chang [5], I-Jan Chen [6], Chengpo Hsu [7] and Tzu-Sen Yang [8,9,10,*]

1   School of Dental Technology, Taipei Medical University, Taipei 11031, Taiwan; apon@tmu.edu.tw (P.-W.P.); weiwei@tmu.edu.tw (W.-F.L.)
2   Graduate Institute of Nanomedicine and Medical Engineering, Taipei Medical University, Taipei 11031, Taiwan; Yang820065@tmu.edu.tw
3   Division of Oral and Maxillofacial Surgery, Department of Dentistry, Wan Fang Hospital, Taipei 11696, Taiwan; ndmcd52@gmail.com
4   School of Dentistry, College of Oral Medicine, Taipei Medical University, Taipei 11031, Taiwan
5   Taiwan Instrument Research Institute, National Applied Research Laboratories, Hsinchu 300, Taiwan; gmp@narlabs.org.tw
6   SouthPort Co., Taipei 110, Taiwan; ijanpaulchen@gmail.com
7   Department of Dental Medicine, Matsumoto Dental University, Shiojiri 399-0704, Japan; bruce951421@hotmail.com
8   Graduate Institute of Biomedical Optomechatronics, Taipei Medical University, Taipei 11031, Taiwan
9   International PhD Program in Biomedical Engineering, Taipei Medical University, Taipei 110, Taiwan
10 Research Center of Biomedical Devices, Taipei Medical University, Taipei 11031, Taiwan
*   Correspondence: tsyang@tmu.edu.tw

Abstract: Selective laser melting (SLM) is extensively used for fabricating metallic biomedical products. After 3D printing, it is almost always advisable to apply a heat treatment to release the internal tensions or optimize the mechanical properties of the printed parts. The aim of this paper is to investigate the effects of heat treatment of SLM printed Ti-6Al-4V (Ti64) circular specimens on the areal surface texture parameters and cell attachment. Areal surface texture parameters, including the arithmetic mean height (S_a), root-mean-square height (S_q), skewness (S_{sk}), and kurtosis (S_{ku}) were characterized. In addition, wavelet-based multi-resolution analysis was applied to investigate the characteristic length scales of untreated and heat-treated Ti64 specimens. In this study, the vertical distance between the highest and lowest position of cell attachment for each sampling area was defined as ΔH. Results showed that an increase in the periodic characteristic length scale was primarily due to the formation of large-scale aggregations of Ti64 metal powder particles on the heat-treated surface. In addition, MG-63 cells preferred lying in concave hollows; in heat-treated specimens, values of ΔH statistically significantly decreased from 31.6 ± 4.2 to 8.8 ± 2.8 µm, while S_{ku} decreased from 3.3 ± 1.4 to 2.6 ± 0.6, indicating a strong influence of S_{ku} on cell attachment.

Keywords: selective laser melting; heat treatment; surface texture; Ti-6Al-4V alloy; cell attachment; microstructure

1. Introduction

Selective laser melting (SLM), an additive manufacturing process, is widely used in metal three-dimensional (3D) printing, where a high-energy laser beam is used to fuse metal powder particles and build a 3D component layer by layer [1–4]. SLM is an advanced method for producing biomedical devices, which are commonly fabricated from Co-Cr-Mo alloys and Ti-6Al-4V (Ti64) alloys due to their excellent mechanical properties and corrosion/wear resistance [5–8]. However, steep thermal gradients are caused by the rapid melting and high solidification rates in the printing phase; this can lead to high residual

stress formation in the printed parts [9,10]. Therefore, heat treatment in the postprinting phase is of particular importance to release the internal tensions and to optimize the mechanical properties of the printed components [11].

Recent in vitro study has shown that mammalian fibroblast cells do not accumulate in the residual stress zone [12]. It is recognized that subjecting SLM-printed specimens to heat treatment is an important step in improving the cytocompatibility, because it minimizes residual stresses and homogenizes metallic microstructures [10,13–15]. In addition, surfaces with high roughness values lead to better interlocking reactions in the implant bone interface zone than do smooth surfaces [16]. Many reports have proven that titanium and its alloys prepared using SLM methods improve osseointegration [17,18].

Previous studies have indicated that surface characteristics, including surface roughness, surface morphology, and contact angle, are crucial in osseointegration and implant infections [19,20]. Another important issue that is still not well understood is the effect of surface roughness features on cell proliferation and attachment. A recent in vitro study found that when the average roughness (Ra) was <24.9 μm, surface roughness promoted the proliferation and differentiation of human osteoblasts [21].

For assessing surface topography, the surfaces' roughness can be quantified using either 2D profile-based or 3D area-based roughness measurements, where the ISO (international organization for standardization) specification standards ISO 4287 [22] and ISO 25178-2 [23] define profile and areal parameters, respectively. Although the industry still uses mainly profile parameters to characterize the topographies, there is a demand for areal parameters for the characterization of specific features [24,25].

In metrology, the surface topography is generally classified into form, waviness, and roughness [26]. Both form and waviness measurements measure the large-scale variations in the surface's height, while surface roughness measurement is of the small-scale variations. Besides, the roughness is measured by subtracting the form and waviness components from the surface's actual contour, where this subtraction is achieved through a digital filter, usually a Gaussian filter [26,27]. Recently, to examine and measure the topography at different length scales, multiscale evaluations such as wavelet, fractal, modal, or Fourier analyses are used to determine these scales for surfaces made by additive manufacturing [28].

In this study, areal surface texture parameters, including the arithmetic mean height (S_a), root-mean-square height (S_q), skewness (S_{sk}), and kurtosis (S_{ku}), were characterized. The wavelet-based multi-resolution analysis was applied to investigate the characteristic length scales of untreated and heat-treated Ti64 specimens. Besides, a Gaussian high-pass filter was used to compare areal surface texture parameters via the measured surface in the absence and filtering presence and assess the effect of unmelted and partially melted Ti64 metal powder particles on these surface texture parameters. On the other hand, the influence of areal surface texture parameters on cell attachment has not yet been reported. Therefore, this study investigates the effects of heat treatment of SLM-fabricated Ti64 specimens on the surface morphology, areal surface texture parameters, contact angles, and cell attachment crucial in osseointegration. The use of areal surface texture parameters can be extended to explore the relationship between areal roughness parameters and cell attachment.

2. Materials and Methods

2.1. Materials and Samples Preparation

The circular Ti64 specimens (10 mm in diameter, 1 mm thick) were manufactured on a Renishaw AM250 SLM system, using Renishaw-provided Ti64 powder with a mean particle size of 30 μm. The Renishaw AM250 system operates a 200-W, 905-nm laser, with respective laser point distance and layer thickness of 50 and 60 μm. 3D-printed Ti64 specimens, without and with heat treatment, were used to investigate the effect of heat treatment on the surface roughness of those specimens. Half of the 3D-printed Ti64 specimens were heated to 600 °C (at 10 °C/min), held at this temperature for 1 h, annealed

at 820 °C (at 10 °C/min), held at this temperature for 4 h, and then slowly cooled to room temperature (RT) inside the furnace.

2.2. Microstructure and Surface Feature Analysis

To characterize the individual particles to build up a distribution, the static imaging method was applied in this study. The Ti64 powders were uniformly immobilized on coverslip, and then the assembled chamber was placed on the microscope stage. High resolution bright field images of Ti64 powders were obtained with an inverted microscope (TE2000U, Nikon, Japan) equipped with an objective lens (Plan Apo 60×/1.40NA oil, Nikon) and an EMCCD camera (Luca^{EM} DL6581, Andor). These images were then processed using ImageJ software to assess the particle size distribution.

Surface morphological characteristics of the untreated and heat-treated Ti64 specimens were observed by a JEOL JSM-6500F scanning electron microscope (SEM; Tokyo, Japan) at an operating voltage of 5 kV. The chemical compositions of SLM-produced Ti64 specimens were analyzed using SEM-EDS. The result showed that the compositions in wt.% for SLM Ti64 specimens comprised 90.46% titanium, 5.94% aluminum, and 3.60% vanadium, indicating that the alloying element compositions were not affected by SLM.

Untreated and heat-treated Ti64 specimens were further characterized under a JadeSurf laser confocal 3D profiler equipped with a 50x/0.75NA objective lens (Southport, Taipei, Taiwan); five different interrogation areas with a square field of view (FOV) of 146.52 × 146.52 μm were chosen and scanned to obtain a 3D surface profile. Here, the surface height was measured point- by- point with 295 nm data spacing.

According to ISO 25178-3, surface roughness measurement usually requires removing the waviness portion from the measured surface to focus on the surface features of interest. Because waviness is mostly more or less periodic irregularities of a workpiece surface with spacings greater than the spacings of its roughness, the recommended minimum cut-off value is 0.1 mm for surface texture. In this study, to assess the effect of unmelted and partially melted Ti64 metal powder particles on surface texture parameters, a Gaussian high-pass filter with a cut-off value of 0.1 mm was used to suppress the longer wavelength components for determining the surface features. This allowed us to compare the areal surface texture parameters via the measured surface in the absence and filtering presence. Both construction of a Gaussian high-pass filter and analysis of 3D surface texture parameters, including the S_a, S_q, S_{sk}, and S_{ku}, were conducted with Matlab software.

2.3. Wavelet Transforms of the Surface Profiles

Wavelet-based multi-resolution analysis was further applied to investigate the characteristic length scales of untreated and heat-treated Ti64 specimens. Previously, wavelets have been applied for surface analysis to find discontinuities, edge, and isolate and analyze surface components [29–31]. In this study, a continuous 1D complex-valued Morlet wavelet was applied to transform these height signals obtained from 3D surface measurements, so that surface features at different length scales can be extracted and quantified. According to Farge [32], the wavelet transform coefficient $W(a, b)$ of a continuous real-valued signal, such as the height signal $H(x)$, can be defined as the inner product between $H(x)$ and an analyzing wavelet $W(a, b) = \int_{-\infty}^{\infty} H(x)\varnothing_{a,b}^*(x)dx$, where $\varnothing_{a,b}^*(x) = (1/\sqrt{a})\varnothing((x - b)/a)$, a and b are respectively the space dilatation and translation parameters, and the asterisk of $\varnothing$ represents the complex conjugate. The corresponding complex-valued 'Morlet' wavelet is $\varnothing(x) = \left(e^{i\omega_0 x}\right)\left(e^{-x^2/2}\right)$ and in this study, we set $\omega_0 = 2\pi$ [33]. Note that the analyzing wavelet $\varnothing_{a,b}(x)$ is a dilatated and translated version of a mother wavelet $\varnothing(x)$ with resolution a^{-1} and position b [32]. The spatial wavelet coefficient $W(a, b)$ provides the strength information of the height signal, and gives the phase information in space domains. Since the Morlet wavelet can identify the local energy density at each given scale, the characteristic scales of surface features may be analyzed. As $W(a, b)$ was obtained, the effective wavelet energy spectrum in the space domain can be defined as

$E_w(a) = \frac{1}{L}\int_0^L |W(a,b)|^2 db$, where L is the total sampling length of the height signal $H(x)$ for untreated and heat-treated specimens.

2.4. Surface Wettability Analysis

To confirm the surface wettability, the sessile liquid drop method was taken to determine the contact angle. The surface contact angle measurements were conducted at room temperature, and one microliter distilled water droplet was used. The measurement was repeated three times with the untreated and heat-treated Ti64 specimens.

2.5. Cell Proliferation Assay

A 3-(4,5-dimethylthiazol-2-yl)-2,5-diphenyltetrazolium-bromide (MTT) assay was used to evaluate cell viability of osteoblast-like human MG63 cells attached to untreated and heat-treated Ti64 specimens after 4, 24, and 72 h of incubation. Human MG-63 osteoblast-like cells were purchased from Bioresource Collection and Research Center (product No. BCRC 60279, BCRC, Hsinchu City, Taiwan).

MG-63 cells were cultured up to $\approx$60% confluence in Dulbecco's modified Eagle medium (DMEM) containing 10% heat-inactivated fetal bovine serum (FBS). Cultures of MG-63 cells were maintained at 37 °C in a humid atmosphere of 5% CO_2. MG-63 cells were trypsinized, counted, and resuspended at the appropriate densities ($\approx 10^5$ cells/mL) in fresh culture medium. All of the Ti64 disks were autoclaved, rinsed with phosphate-buffered saline (PBS), and transferred to 24-well tissue culture plates. Prior to cell seeding, specimens were equilibrated in culture medium for 10 min. Subsequently, MG-63 cells were drop-seeded onto substrates at a density of 5×10^4 cells/mL and incubated statically for at least 1 h to allow cell attachment. At specified time intervals of cultivation, namely 4, 24, and 72 h of incubation, an MTT (0.5 mg/mL) solution was added to each well, and cells were further incubated for 3 h at 37 °C. Supernatants were removed, and 1000 μL of dimethyl sulfoxide (DMSO) was added to each well to dissolve the formazan product. Then, 100 μL of supernatant from each well was transferred to new 96-well cell culture plates. Absorbance at 570 nm was measured using an enzyme-linked immunosorbent assay (ELISA) reader. Five parallel specimens were used to provide an average and standard deviation (sd).

2.6. Immunofluorescence

To further observe the location of MG-63 cells attached to specimens, MG-63 cells were drop-seeded onto substrates at a density of 5×10^4 cells/mL. After 72 h of incubation, MG-63 cells were separately fixed with 4% paraformaldehyde (PFA) for 15 min and permeabilized with 0.1% Triton X-100 for 5 min at RT. Subsequently, samples were washed with PBS three times. Finally, cell nuclei were stained with 1 μg/mL propidium iodide (PI) for 30 min at RT. Fluorescence images of cells were obtained with an inverted microscope (TE2000U, Nikon, Japan) equipped with an objective lens (Plan Fluro 40×/0.6NA, Nikon) and an EMCCD camera (Luca^EM DL6581, Andor).

2.7. Statistical Analysis

All data were expressed as means $\pm$ sd. One-way analysis of variance (ANOVA) with Tukey HSD (honestly significant difference) post-hoc test was used to assess differences among the groups; $p < 0.05$ and $p < 0.01$ were considered statistically significant and statistically highly significant, respectively.

3. Results and Discussion

3.1. Ti64 Powdersize Distribution

Figure 1 shows the morphologies and the particle size distribution of Ti64 powders. The powders are nearly spherical, and the mean particle size of the Ti64 powders determined using ImageJ was 31.42 $\pm$ 9.27 μm (n = 116, mean $\pm$ sd) which is consistent with the

Renishaw-provided Ti64 powder with a mean particle size of 30 μm as described by the manufacturer to have particles with diameters in the range 16–45 μm [34].
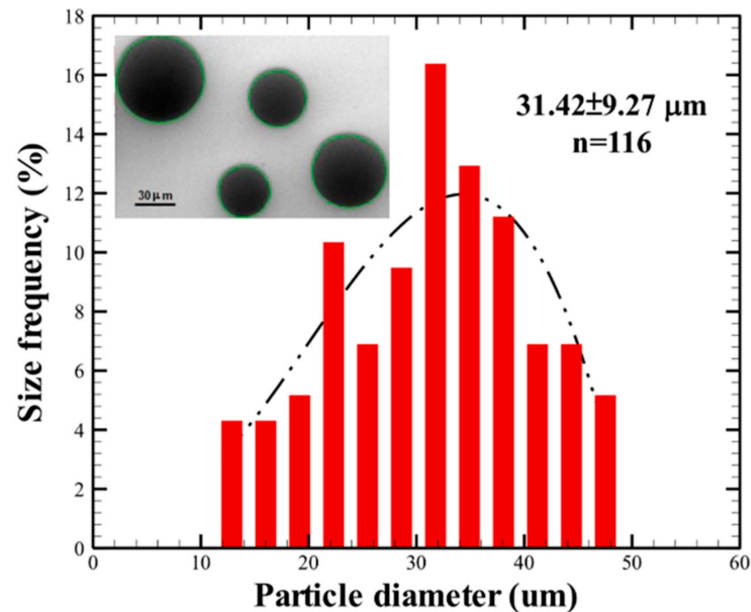
Figure 1. Optical microscope image and the particle size distribution of Ti64 powder. The mean particle size of the Ti64 powders determined using ImageJ was 31.42 ± 9.27 μm ($n = 116$).

3.2. Surface Morphology and Roughness Analysis

In a low-magnification SEM image (100×) in Figure 2a, microtexturing is evident on the surface of the Ti64 specimens, where unmelted Ti64 metal powder particles were sintered to the surface of the structure during manufacturing. In Figure 2d, heat treatment caused some of the unmelted and partially melted Ti64 metal powder particles to become further fused and bonded to the surface. Moderately magnified images (1000×) (Figure 2b,e) further revealed a distinct difference between the two surfaces: when the 3D-printed Ti64 specimen was annealed at 820 °C, heat treatment led to the formation of large-scale aggregations of Ti64 metal powder particles (Figure 2e) compared to the surface of control specimens. In higher-magnification images ($10^4 \times$) in Figure 2c,f, nanotexturing is evident on the surface of the heat-treated Ti64 specimens, which revealed a difference at the nanometer scale, namely, a closely spaced lattice layer formed on heat-treated specimens, which resulted in nano-elevation of the surface roughness.
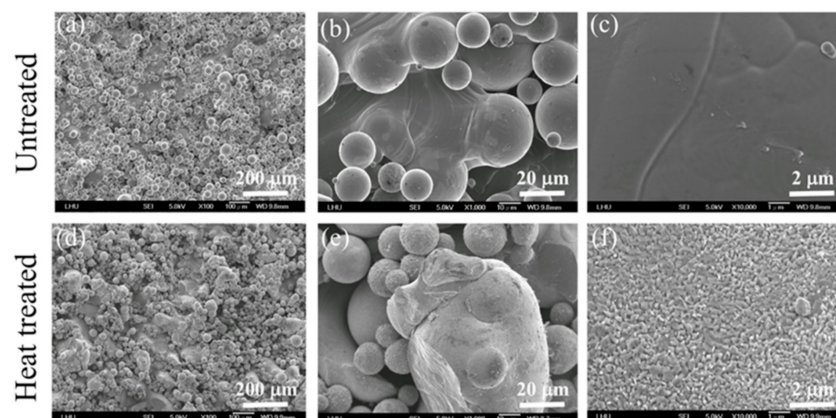
Figure 2. SEM micrographs of untreated and heat-treated Ti64 specimens at different magnifications. (**a**,**d**) 100×; (**b**,**e**) 1000×; (**c**,**f**) $10^4 \times$.

As can be seen in Figure 2, the untreated 3D-printed Ti64 specimen primarily consists of microscale features (unmelted and partially melted Ti64 metal powder particles); however, the surface of a heat-treated specimen had a hierarchical structure consisting of microscale features (partially melted Ti64 spheroids) and nanoscale features (closely spaced nano-lattices). It was suggested that roughness in the micrometer range provides better biomechanical interlocking, while roughness in the nanometer range provides more adhesion sites for extracellular matrix (ECM) proteins [35]. The present experimental evidence possibly support why heat-treated SLM specimens are thought to promote implant stabilization and osseointegration.

Figure 3a–e,g–k respectively show 3D surface topographies of untreated and heat-treated Ti64 specimens, where the surface height was measured using a laser confocal 3D profiler. To provide an easily interpreted encoding of surface heights, Parula mapping of height to color varying from blue to yellow was used in the current figure. Five interrogation areas with a FOV of 146.52 × 146.52 μm were scanned on each Ti64 specimen, as illustrated in Figure 3f,l. In the case of the untreated 3D-printed Ti64 specimen, yellow areas represent locations of unmelted Ti64 metal powder particles sintered to the surface, where the diameter of the yellow areas was of the same order as that of Ti64 powder, as shown in Figure 3a–e. In contrast, the formation of large-scale aggregations of Ti64 metal powder particles can be seen on the heat-treated surface, as shown in the large yellow areas in Figure 3i,k. As can be seen in Figure 3, the 3D surface topography depicted the same microscale features as did the SEM images.
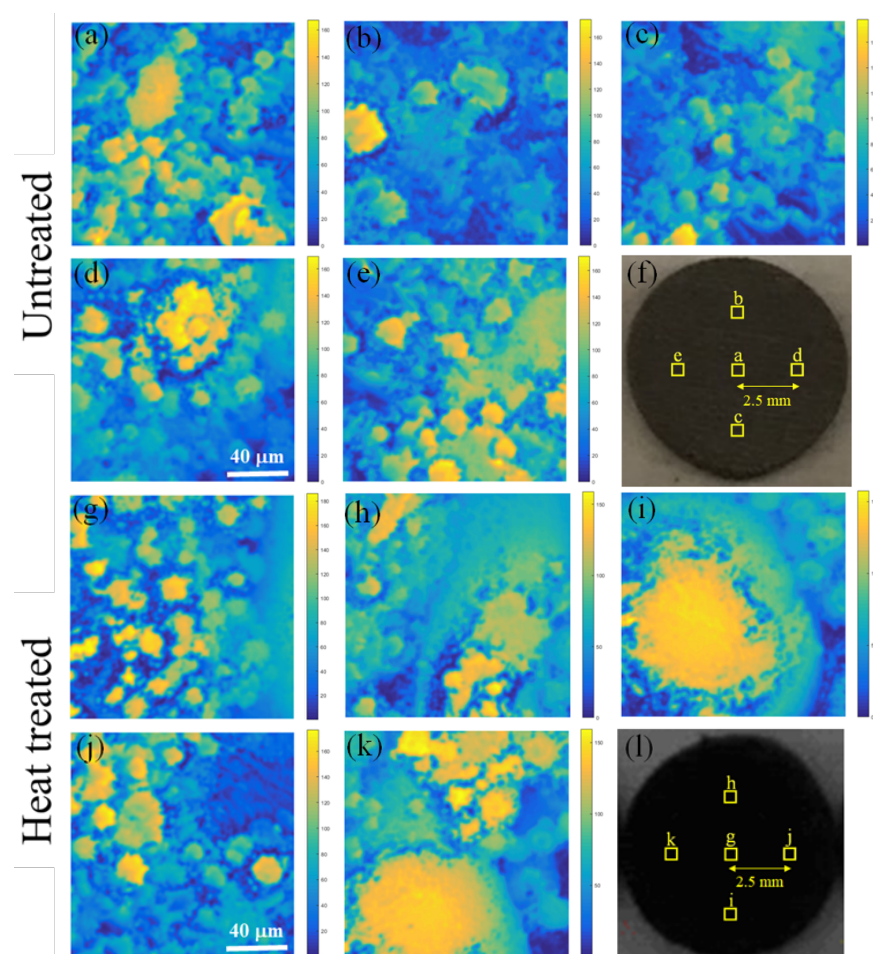

Figure 3. 3D surface topographies of Ti64 specimens measured using a laser confocal 3D profiler. (**a**–**e**)/(**g**–**k**) Surface heights of untreated/heat-treated Ti64 specimens; (**f**,**l**) untreated and heat-treated Ti64 specimens, where five interrogation areas equally spaced on each Ti64 specimen were selected for surface height measurements.

In this study, a Gaussian high-pass filter with a cut-off value of 0.1 mm was used to obtained roughness and waviness features. Figure 4a–f respectively show the real surfaces, the roughness features, and the waviness features of untreated/heat-treated Ti64 specimens, where the real surface data were directly obtained from the position (a) and position (i) (see Figure 3). The results showed that the waviness features were directly due to the presence of unmelted and partially melted Ti64 metal powder particles sintered to the surface. As can be seen, the large-scale variations in the surface's height, such as form and waviness, should be neglected as the length scale of FOV is similar to the minimum cut-off value of 0.1 mm. Therefore, this small evaluation length (146.52 μm), about five times the mean particle size of the Ti64 powders, allows us to directly valuate the areal roughness parameters from the SLM printed Ti-6Al-4V surface's actual contour.
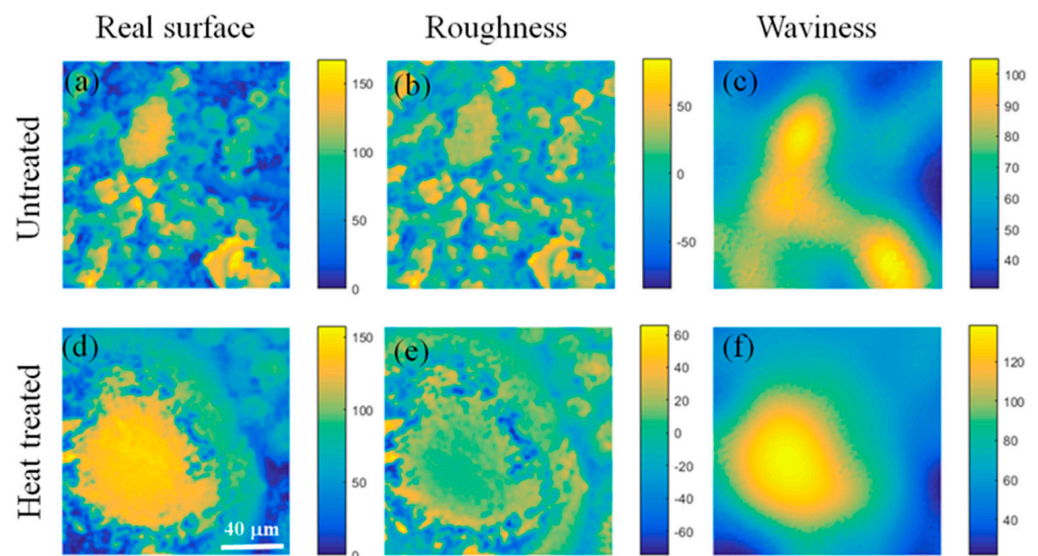
Figure 4. A Gaussian high-pass filter with a cut-off value of 0.1 mm was used to suppress the longer wavelength components for determining the surface features. (**a**–**c**)/(**d**–**f**) respectively show the real surfaces, the roughness features, and the waviness features of untreated/heat-treated Ti64 specimens.

Figure 5 shows the 3D surface texture parameters, including S_a, S_q, S_{sk}, and S_{ku}, for untreated and heat-treated specimens, where the corresponding values of p are 0.14, 0.06, 0.02, and 0.04, respectively. As can be seen, values of S_a and S_q were not sensitive to the surface topography of the untreated or heat-treated Ti64 specimens; however, values of S_{sk} and S_{ku} revealed distinct differences between the two surfaces. The heat-treated sample had an S_{sk} value of 0.3 ± 0.2, which is within the range of $-\frac{1}{2}$ and $+\frac{1}{2}$; i.e., the height distribution was approximately symmetrical. However, the untreated sample had an S_{sk} value of 0.7 ± 0.2, which is within the range of $+\frac{1}{2}$ and $+1$; i.e., the height distribution was moderately skewed. On the other hand, the heat-treated sample had an S_{ku} value of 2.6 ± 0.3, which is smaller than 3, and so the height distribution curve is said to be platykurtic and have relatively few high peaks or low valleys. However, the untreated sample had an S_{ku} value of 3.3 ± 0.6, which is larger than 3, and so the height distribution is spiked, and the surface has relatively many high peaks and low valleys. Accordingly, this finding also depicts the same microscale features as SEM images.
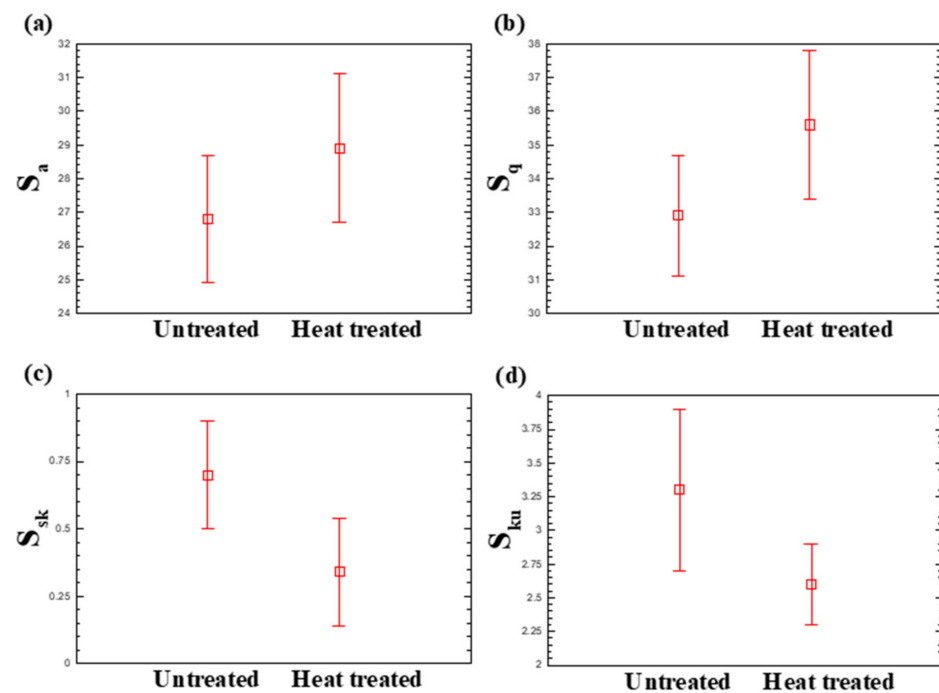
Figure 5. 3D surface texture parameters, including (**a**) S_a, (**b**) S_q, (**c**) S_{sk}, and (**d**) S_{ku}, for untreated and heat-treated Ti64 specimens.

Roughness features obtained by a high-pass filter with a cut-off value of 0.1 mm were further analyzed to compare the areal surface texture parameters via the measured surface in the absence and filtering presence. Table S1 showed that after removing the waviness portion from the measured surface, values of S_a, S_q, and S_{ku} were not sensitive to the surface topography of the untreated or heat-treated Ti64 specimens, where the corresponding values of p are 0.94, 0.66, and 0.35, respectively; however, the value of S_{sk} revealed distinct differences between the two surfaces ($p < 0.01$). After removing the waviness portion from the measured surface, values of S_{sk} for the untreated sample and the heat-treated sample were 0.4 ± 0.1 and 0.0 ± 0.2, respectively, which was within the range of $-\frac{1}{2}$ and $+\frac{1}{2}$; i.e., the height distribution was approximately symmetrical. Interestingly, values of S_{sk} for untreated and heat-treated Ti64 specimens were larger than 3, which implied the surface has relatively high peaks and low valleys. As can be seen in Figure 4, these spikes were localized around the surface of the unmelted and partially melted Ti64 metal powder particles. These spikes' contribution to the S_{sk} became significant after removing the waviness portion from the measured surface.

Although a Gaussian high-pass filter with a cut-off value of 0.1 mm could be used to suppress the longer wavelength components for determining the surface features, this could also remove the surface features due to the presence of unmelted and partially melted Ti64 metal powder particles sintered to the surface. Note that in this study, the length scale of FOV was similar to the minimum cut-off value of 0.1 mm, and therefore by using small sampling lengths during measurement, it should be possible to obtain accurate values of the S_{sk} and S_{ku} [24]. For this reason, this study primarily focused on the areal surface texture parameters via the measured surface in the absence of a Gaussian high-pass filtering to address the effect of heat treatment of SLM printed Ti64 specimens on cell attachment.

3.3. Surface Morphology and Roughness Analysis

Figure 6a–f respectively show the height signals, contour plots of the wavelet transform of the height signals, and the average wavelet spectra of untreated/heat-treated Ti64 specimens, where the height signals were directly obtained along the horizontal axis from the symmetry center of the position (a) and position (g) (see Figure 3). In Figure 6b,e, the

abscissa is the sampling length, the ordinate represents the characteristic length scales, and the color bar indicates the magnitude of the wavelet coefficient $W(a, b)$. As can be seen from these two figures, there are multi characteristic scales that reveal periodic oscillations for the height signals. For the case of untreated Ti64 specimen (Figure 6c), there existed a small characteristic period around 14 μm, which is smaller than the mean particle size of the Ti64 powders. Besides, there existed characteristic scales around 29 and 45 μm, respectively, which were in the range of 1–2 powder sizes. Besides, there also existed a large periodic characteristic scale around 84 μm, which is more than twice of the mean particle size of the Ti64 powders. As discussed in Figure 2a, unmelted Ti64 metal powder particles were sintered to the structure's surface during manufacturing. We speculated that there might exist powder-size subpopulations. When these subpopulations are uniformly distributed and sintered to the surface, periodic characteristic scales appeared and could be decomposed via the wavelet transform of the height signals.
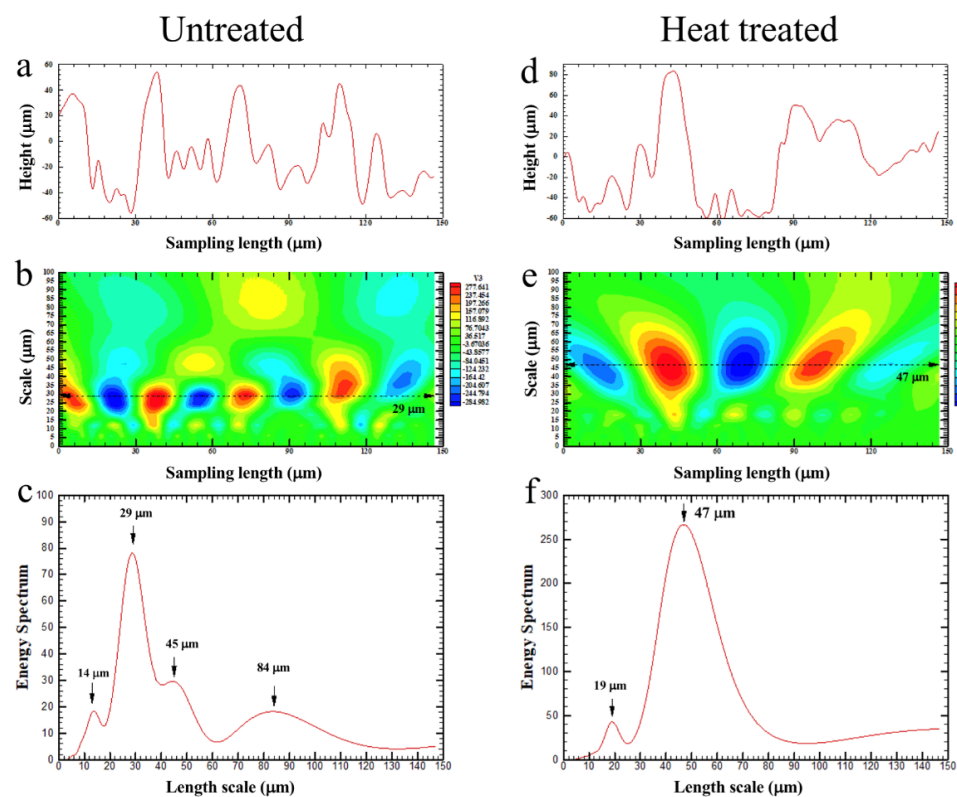
Figure 6. Wavelet-based multi-resolution analysis for the characteristic length scales of untreated and heat-treated Ti64 substrates. (**a**–**c**)/(**d**–**f**) respectively show the height signals, contour plots of the wavelet transform of the height signals, and the average wavelet spectra of untreated/heat-treated Ti64 specimens, where the height signals were directly obtained along the horizontal axis from the symmetry center of the position (a) and position (g) (see Figure 3).

For the case of heat-treated Ti64 specimen (Figure 6f), there existed characteristic scales around 19 and 47 μm, respectively, where the former was smaller than the powder diameter and the latter was in the range of 1–2 powder sizes. Therefore, we focus on calculating periodic characteristic scales that appear in the range of 1–2 powder sizes, and define the mean value of the periodic characteristic scales as the primary peak. The results showed that for heat-treated specimens, the value of the primary peak statistically significantly increased from 37.4 ± 3.8 to 45.6 ± 6.9 μm ($n = 5$, $p = 0.048$), which revealed that an increase in the periodic characteristic length scale was primarily due to the formation of large-scale aggregations of Ti64 metal powder particles on the heat-treated surface, as discussed in Figure 2d,e.

3.4. Surface Wettablity Analysis

To confirm the surface wettability, contact angle measurements were taken. As can be seen in Figure S1, all Ti64 specimens were found to be hydrophobic, where the contact angles for untreated and heat-treated Ti64 specimens were $126.4° \pm 1.4°$ and $130.7° \pm 2.3°$, respectively ($p = 0.05$). The slightly increase in hydrophobicity for heat-treated Ti64 specimens was most likely due to the presence of air pockets created by the formation of large-scale aggregations of Ti64 metal powder particles on the heat-treated surface [36]. The hydrophobic property of SLM-fabricated Ti64 specimens was consistent with previous result by A. Sarker et al. [36], but contrary to that obtained by M. Wang et al. [10].

3.5. Cell Viability Analysis

The cell viability of MG-63 cells attached to untreated/heat-treated Ti64 specimens after 4, 24, and 72 h of incubation was examined using an MTT assay (Figure 7). Compared with untreated specimens, MG-63 cells attached to the heat-treated surface showed a statistically significant difference in viability after 4 and 24 h of incubation, which implied the heat-treated surface promoted rapid cell attachment. After 72 h of incubation, the proliferation for MG-63 cells attached on the heat-treated surface was still high, but the difference was not statistically significant ($p = 0.08$). These results indicating that heating process could enhance the cell proliferation due to the promotion of attachment of MG-63 cells especially occurred in the initial 4 h of cell attachment.
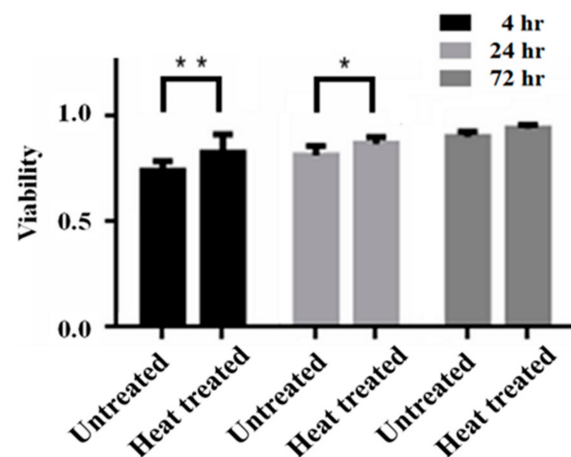

Figure 7. Determination of cell viability by an MTT assay. The MTT assay was performed to evaluate cell viability of osteoblast-like human MG-63 cells attached to untreated and heat-treated Ti64 substrates after 4, 24, and 72 h of incubation ($n = 5$, *, $p < 0.05$; **, $p < 0.01$).

3.6. Cell Adhesion Analysis

MG-63 cells were stained with PI dye to explore the relationship between the surface texture parameters and cell attachment. We used the $40\times$ objective lens in the absence and presence of $1.5\times$ intermediate magnification to visualize MG-63 cells attached to the untreated and heat-treated Ti64 specimens. Fluorescence images of cell nuclei were applied to identify the vertical distance (ΔH) between the highest and lowest position of MG-63 cells attached to the specimens, where values of ΔH were identified via adjusting the objective lens in the vertical direction (see also Movie S1). Here, ten sets of fluorescence images were selected on each Ti64 specimen, and three sets of these images are shown in Figure 8. Figure 8a–l respectively show the highest/lowest positions of MG-63 cells attached to untreated and heat-treated Ti64 specimens. As can clearly be seen in Figure 8, MG-63 cells preferred lying in concave hollows. In addition, the present results showed that for heat-treated specimens, values of ΔH statistically significantly decreased from 31.6 ± 4.2 to 8.8 ± 2.8 μm ($n = 10$, $p < 0.01$) when S_{ku} decreased from 3.3 ± 0.6 (greater than 3) to 2.6 ± 0.3 (less than 3), indicating a strong influence of S_{ku} on cell attachment.

This can simply be understood as the untreated specimen ($S_{ku} > 3$) having relatively many high peaks and low valleys compared to the heat-treated specimen, such that the spatial distribution of cells in the vertical direction had a greater degree of change. This finding suggests that 3D surface texture parameters can be employed to provide greater insights into relationships between surface roughness features and cell attachment.
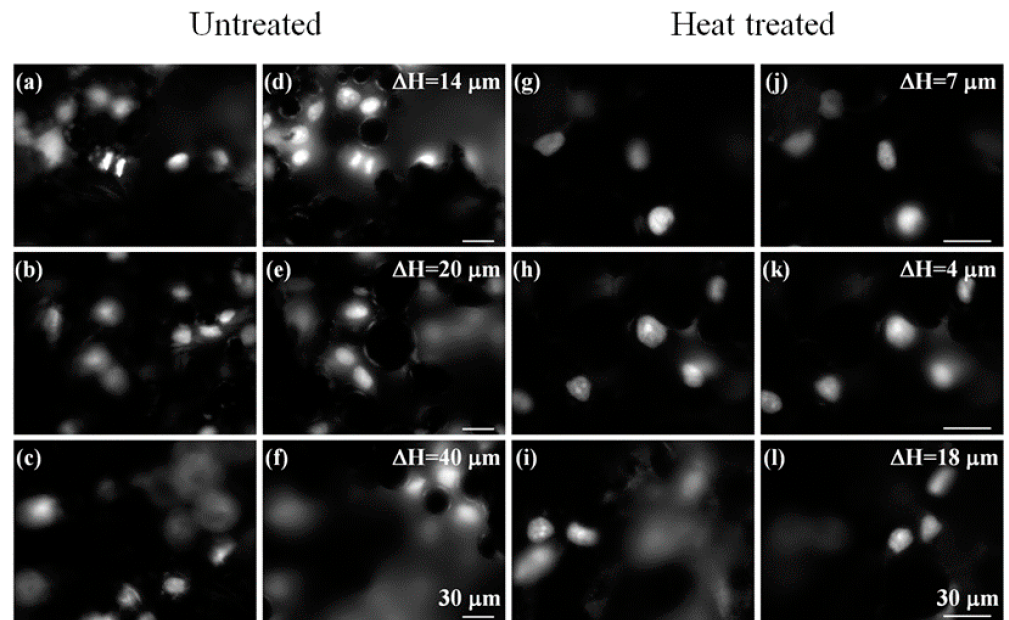
Figure 8. Fluorescence images of MG-63 cells attached to Ti64 specimens (cell nuclei stained with PI). (**a**–**c**)/(**d**–**f**) and (**g**–**i**)/(**j**–**l**) are the highest/lowest positions of MG-63 cells attached to untreated and heat-treated Ti64 specimens, respectively. Scale bar 30 µm.

We adopted a microscopy-based approach to separately map 3D surface topographies of untreated and heat-treated Ti64 specimens and visualizing the highest/lowest MG-63 cells attached to Ti64 specimens, which allowed indirect probing of the relationship between the surface texture parameters and cell attachment in the present work. We are now trying to integrate fluorescence detection into the laser confocal 3D profiler that allows direct probing of both 3D surface topographies and the corresponding MG-63 cell attachment simultaneously.

4. Conclusions

In summary, this study investigated the effects of heat treatment of SLM-fabricated Ti64 specimens on the surface morphology, areal surface texture parameters, and contact angles that are crucial in osseointegration and implant infections. The SEM images showed that the untreated Ti64 specimens primarily consists of microscale features, whereas the surface of a heat-treated specimen had a hierarchical structure consisting of microscale features and nanoscale features. The 3D surface height was measured using a laser confocal 3D profiler to determine the surface texture parameters. Values of S_a and S_q were not sensitive to the surface topography of the untreated or heat-treated Ti64 specimens; however, S_{sk} and S_{ku} revealed distinct differences between the two surfaces. The wavelet-based multi-resolution analysis was applied to investigate the characteristic length scales of untreated and heat-treated Ti64 specimens. Both Ti64 specimens revealed periodic oscillations for the height signals. The primary peak value significantly increased from 37.4 ± 3.8 (untreated) to 45.6 ± 6.9 µm (heat-treated) primarily due to the formation of large-scale aggregations of Ti64 metal powder particles on the heat-treated surface. The contact angle measurements revealed all Ti64 specimens were found to be hydrophobic, where the contact angles for untreated and heat-treated Ti64 specimens were $126.4° \pm 1.4°$ and $130.7° \pm 2.3°$, respectively. Compared with untreated specimens, MG-63 cells attached to the heat-treated surface

showed a significant difference in proliferation after 4, and 24 h of incubation. The present results showed a strong influence of kurtosis (S_{ku}) on cell attachment; therefore, 3D surface texture parameters can be extended to explore the relationship between surface roughness and cell attachment. The potential biomedical context of this study is alveolar bone to Ti64 dental implant. We are currently using the proposed a continuous-wave laser-induced forward transfer (CW-LIFT) system [37] for cell printing on the untreated and heat-treated Ti64 specimens for tissue engineering applications, and these results will be reported in the near future.

Supplementary Materials: The following are available online at https://www.mdpi.com/2076-3417/11/5/2234/s1, Figure S1. The wettability of the untreated (left) and heat-treated (right) SLM-fabricated Ti64 specimens. Table S1. The areal surface texture parameters via the measured surface in the filtering presence for untreated and heat-treated Ti64 specimens. Video S1: The real-time fluorescence images of MG-63 cells attached to untreated Ti64 specimens (cell nuclei stained with PI). (AVI).

Author Contributions: Co-first author, J.-C.Y.; Conceptualization, T.-S.Y., P.-W.P. and J.-C.Y.; methodology, C.-M.C.; software, I.-J.C; validation, C.H.; investigation, W.-F.L. and C.-Y.F.; writing—original draft preparation, T.-S.Y.; writing—review and editing, T.-S.Y. All authors have read and agreed to the published version of the manuscript.

Institutional Review Board Statement: Not applicable.

Informed Consent Statement: Not applicable.

Data Availability Statement: Data is contained within the article.

Conflicts of Interest: The authors declare no conflict of interest.

References

1. Vandenbroucke, B.; Kruth, J.P. Selective laser melting of biocompatible metals for rapid manufacturing of medical parts. *Rapid Prototyp. J.* **2007**, *13*, 196–203. [CrossRef]
2. Sidambe, A.T. Biocompatibility of advanced manufactured titanium implants-A review. *Materials* **2014**, *7*, 8168–8188. [CrossRef] [PubMed]
3. Gibson, I.; Rosen, D.W.; Stucker, B. *Additive Manufacturing Technologies*; Springer: Berlin/Heidelberg, Germany, 2010; Volume 238.
4. Thijs, L.; Verhaege, F.; Craeghs, T.; van Humbeeck, J.; Kruth, J.P. A study of the microstructural evolution during selective laser melting of Ti-6Al-4V. *Acta Mater.* **2010**, *58*, 3303–3312. [CrossRef]
5. Kok, Y.; Tan, X.P.; Wang, P.; Nai, M.L.S.; Loh, N.H.; Liu, E.; Tor, S.B. Anisotropy and heterogeneity of microstructure and mechanical properties in metal additive manufacturing: A critical review. *Mater. Des.* **2018**, *139*, 565–586. [CrossRef]
6. Kajima, Y.; Takaichi, A.; Kittikundecha, N. Effect of heat-treatment temperature on microstructures and mechanical properties of Co–Cr–Mo alloys fabricated by selective laser melting. *Mater. Sci. Eng. A* **2018**, *726*, 21–31. [CrossRef]
7. Lee, W.F.; Wang, J.C.; Hsu, C.Y.; Peng, P.W. Microstructure, mechanical properties, and retentive forces of cobalt-chromium removable partial denture frameworks fabricated by selective laser melting followed by heat treatment. *J. Prosthet. Dent..* in press.
8. Peng, P.W.; Hsu, C.Y.; Huang, H.Y.; Chao, J.C.; Lee, W.F. Trueness of removable partial denture frameworks additively manufactured with selective laser melting. *J. Prosthet Dent..* in press.
9. Zavala-Arredondo, M.; Ali, H.; Groom, K.M. Investigating the melt pool properties and thermal effects of multi-laser diode area melting. *Int. J. Adv. Manuf. Technol.* **2018**, *97*, 1383–1396. [CrossRef]
10. Wang, A.M.; Wu, Y.; Lu, S.; Chen, T.; Zhao, Y. Fabrication and characterization of selective laser melting printed Ti–6Al–4V alloys subjected to heat treatment for customized implants design. *Prog. Nat. Sci. Mater. Int.* **2016**, *26*, 671–677. [CrossRef]
11. Beese, A.M.; Carroll, B.E. Review of Mechanical Properties of Ti-6Al-4V Made by Laser-Based Additive Manufacturing Using Powder Feedstock. *JOM* **2016**, *68*, 724–734. [CrossRef]
12. Colpitts, C.; Ektesabi, A.M.; Wyatt, R.A.; Crawford, B.D.; Kiani, A. Mammalian fibroblast cells avoid residual stress zone caused by nanosecond laser pulses. *J. Mech. Behav. Biomed. Mater.* **2017**, *74*, 214–220. [CrossRef]
13. Martin, F.; Konecna, R.; Nicoletto, G. Microstructure and fatigue performance of SLM-fabricated Ti6Al4V alloy after different stress-relief heat treatments. *Transport Res. Procedia* **2019**, *40*, 24–29.
14. Potomati, F.; Giordani, E.J.; Duarte, L.T. Fatigue behavior and physical characterization of surface-modified Ti-6Al-4V ELI alloy by micro-arc oxidation. *Mater. Res. Ibero Am. J. Mater.* **2012**, *15*, 305–311. [CrossRef]
15. Yadroitsev, I.; Krakhmalev, P.; Yadroitsava, I. Selective laser melting of Ti6Al4V alloy for biomedical applications: Temperature monitoring and microstructural evolution. *J. Alloy. Compd.* **2014**, *583*, 404–409. [CrossRef]

16. Wang, Q.; Zhou, P.; Liu, S.; Attarilar, S.; Ma, R.L.W.; Zhong, Y. Multi-scale surface treatments of titanium implants for rapid osseointegration: A Review. *Nanomaterials* **2020**, *10*, 1244. [CrossRef]

17. Ataee, A.; Li, Y.; Wen, C. A comparative study on the nanoindentation behavior, wear resistance and in vitro biocompatibility of SLM manufactured CP–Ti and EBM manufactured Ti64 gyroid scaffolds. *Acta Biomater.* **2019**, *97*, 587–596. [CrossRef] [PubMed]

18. Xiong, Y.; Wang, W.; Gao, R.; Zhang, H.; Dong, L.; Qin, J.; Wang, B.; Jia, W.; Li, X. Fatigue behavior and osseointegration of porous Ti-6Al-4V scaffolds with dense core for dental application. *Mater. Des.* **2020**, *195*, 108994. [CrossRef]

19. Elias, C.N.; Oshida, Y.; Lima, J.H.; Muller, C.A. Relationship between surface properties (roughness, wettability and morphology) of titanium and dental implant removal torque. *J. Mech. Behav. Biomed. Mater.* **2008**, *1*, 234–242. [CrossRef]

20. Lin, N.; Li, D.; Zou, J.; Xie, R.; Wang, Z.; Tang, B. Surface texture-based surface treatments on Ti6Al4V titanium alloys for tribological and biological applications: A mini review. *Materials* **2018**, *11*, 487. [CrossRef]

21. Ponader, S.; Vairaktaris, E.; Heinl, P.; Wilmowsky, C.V.; Rottmair, A.; Körner, C.; Singer, R.F.; Holst, S.; Schlegel, K.A.; Neukam, F.W.; et al. Effects of topographical surface modifications of electron beam melted Ti-6Al-4V titanium on human fetal osteoblasts. *J. Biomed. Mater. Res. A* **2008**, *84*, 1111–1119. [CrossRef]

22. ISO_4287 BE; BS EN ISO_4287. *Geometrical Product Specification (GPS): Surface Texture: Profile Method: Terms, Definitions and Surface Texture Parameters*; British Standards Institute: London, UK, 2000.

23. ISO_25178-2 BE; BS EN ISO_25178-2. *Geometrical Product Specifications (GPS): Surface Texture: Areal 2: Terms, Definitions and Surface Texture Parameters*; British Standards Institute: London, UK, 2012.

24. Hansson, K.N.; Hansson, S. Skewness and kurtosis: Important parameters in the characterization of dental implant surface roughness—A computer simulation. *ISRN Mater. Sci.* **2011**, *2011*, 1–6. [CrossRef]

25. Olivares-Navarrete, R.; Hyzy, S.L.; Berg, M.E. Osteoblast Lineage Cells Can Discriminate Microscale Topographic Features on Titanium–Aluminum–Vanadium Surfaces. *Ann. Biomed. Eng.* **2014**, *42*, 2551–2561. [CrossRef]

26. Eseholi, T.; Coudoux, F.-X.; Corlay, P.; Sadli, R.; Bigerelle, M. A Multiscale Topographical Analysis Based on Morphological Information: The HEVC Multiscale Decomposition. *Materials* **2020**, *13*, 5582. [CrossRef] [PubMed]

27. Newton, L.; Senin, N.; Chatzivagiannis, E.; Smith, B.; Leach, R. Feature-based characterisation of Ti6Al4V electron beam powder bed fusion surfaces fabricated at different surface orientations. *Addit. Manuf.* **2020**, *35*, 101273.

28. Brown, C.A.; Hansen, H.N.; Jiang, X.; Blateyron, F.; Berglund, J.; Senin, N.; Bartkowiak, T.; Dixon, B.; Goïc, G.L.; Quinsat, Y.; et al. Multiscale Analyses and Characterizations of Surface Topographies. *CIRP Ann.* **2018**, *67*, 839–862. [CrossRef]

29. Workman, M.J.; Serov, A.; Halevi, B.; Atanassov, P.; Artyushkova, K. Application of the discrete wavelet transform to SEM and AFM micrographs for quantitative analysis of complex surfaces. *Langmuir* **2015**, *31*, 4924–4933. [CrossRef] [PubMed]

30. Maksumov, A.; Vidu, R.; Palazoglu, A.; Stroeve, P. Enhanced feature analysis using wavelets for scanning probe microscopy images of surfaces. *J. Colloid Interface Sci.* **2004**, *27*, 365–377. [CrossRef] [PubMed]

31. Sun, W.; Mukherjee, R.; Stroeve, P.; Palazoglu, A.; Romagnoli, J.A. A multi-resolution approach for line-edge roughness detection. *Microelectron. Eng.* **2009**, *86*, 340–351. [CrossRef]

32. Farge, M. Wavelet transforms and their applications to turbulence. *Ann. Rev. Fluid Mech.* **1992**, *24*, 395–456. [CrossRef]

33. Yang, T.S.; Shy, S.S. Two-way interaction between solid particles and homogeneous air turbulence: Particle settling rate and turbulence modification measurements. *J. Fluid Mech.* **2005**, *526*, 171. [CrossRef]

34. Clark, N.; Jones, N.; Porch, A. Measurement of average particle size in metal powders by microwave cavity perturbation in the magnetic field. *Sens. Actuators A* **2017**, *259*, 137–143. [CrossRef]

35. Albrektsson, T.; Wennerberg, A. On osseointegration in relation to implant surfaces. *Clin. Implant. Dent. Relat. Res.* **2019**, *21* (Suppl. 1), 4–7. [CrossRef] [PubMed]

36. Sarker, A.; Tran, N.; Rifai, A.; Brandt, M.; Tran, P.; Leary, M.; Fox, K.; Williams, R. Rational design of additively manufactured Ti6Al4V implants to control Staphylococcus aureus biofilm formation. *Materialia* **2019**, *5*, 100250. [CrossRef]

37. Huang, C.F.; Colley, M.M.S.; Lu, L.S.; Chang, C.Y.; Peng, P.W.; Yang, T.S. Performance characterization of continuous-wave laser-induced forward transfer of liquid bioink. *Appl. Phys. Express* **2019**, *12*, 116504. [CrossRef]